Title: Theory analysis of the optical mode localized sensing based on coupled ring resonators

Authors: Yu Feng,Shumeng Wang,Goran Mashanovich,Jize Yan

Accepted: 13 August 21

Posted 18 August 21

DOI: https://doi.org/10.1364/OE.434400

Theory analysis of the optical mode localized sensing based on coupled ring resonators

Yu Feng,[1*], Shumeng Wang,[1] Goran Mashanovich,[2] and Jize Yan[1*]

[1] *Electronics and Computer Science, University of Southampton, Southampton SO17 1BJ, U.K*
[2] *Optoelectronics Research Centre, University of Southampton, Southampton SO171BJ, U.K.*
[*] *yf1g15@soton.ac.uk; J.Yan@soton.ac.uk*

Abstract: Based on Mason's signal flow graph analysis, an analytical model of the optical mode localization based on coupled ring resonators is established. The correctness of the theoretical model is proved by simulation. High sensitivity and common-mode rejection can be achieved by evaluating the modal power ratio from resonant peaks as sensing output. Based on the four-port structure, two output spectrum with mode localization (asymmetric mode splitting) and symmetric mode splitting allows the high-sensitivity sensing and dual-channel calibration to be carried out simultaneously, which can reduce the sensing errors. Monte-Carlo analysis showed that fabrication imperfection changes less than 6% of the performance in 90% cases, thus the construction of practical sensors is possible with appropriate tuning. The optical mode localized sensing has advantages in sensitivity, accuracy, anti-aliasing compared with conventional micro-mechanical mode localized sensor. Various types of high-sensitive sensor can be constructed through coupling parametric perturbation with measurands in different physical domains.

1. Introduction

The mode localized sensing is first accomplished by coupled micro-electro-mechanical systems (MEMS) resonators. Mode localization MEMS sensors achieve several advantages such as high sensitivity [1] and common-mode rejection [2]. A series of mode localized sensors have been created with incredible sensitivity [3].

For optical systems, resonant mode splitting happens when multiple identical resonators are identically coupled together. Localized perturbation in resonators and couplers will cause the asymmetry in mode splitting. In this case, the total energy in the spectrum will not be evenly confined in all resonant modes of the system, and it results in different modal amplitudes. This is the mode localization phenomenon. The symmetry of the mode splitting can be evaluated by the modal power ratio between different modes that depend on the localized perturbation in effective index and coupling coefficient, thus the localized perturbation can be detected by examining the modal power ratio. Here we name this sensing mechanism as optical mode localized sensing.

This sensing mechanism can be embedded in optical waveguide/fiber systems to develop ultra-sensitive sensors based on mode localization in optically coupled ring resonators. The sensing element of the optical mode localization sensor can be chosen to be constructed from optical ring resonators coupled with each other by directional couplers. The optical structure constructed with coupled ring resonators is referred to as coupled resonator optical waveguide system (CROW) [4]. The existing applications of CROW covers electromagnetic induced transparency, slow light/delay line, gyroscope [5], biosensor and optical communication [6] [7].

The transfer matrix method is widely used in analyzing the spectrum of CROW with identical ring resonators [4] [8]. The numerical computation of the spectrum is effectively simplified by identical electric intensity eigenvectors between adjacent resonators. However, hard work is required to derive the analytical expressions for electrical properties in CROW with non-identical ring resonators. Here we use feedback theory [9] [10] (also referred to as Mason's rule [11] [12]), which makes the analytical derivation easier, to analyze the coupled ring resonators for optical mode localized sensing.

The theoretical model is validated by comparing the calculation results from the theoretical model and simulation (Lumerical connection). There are four parametric configurations with different output characteristics. The mode localization caused by index perturbation (configuration C.) is considered a good choice for constructing the sensing element among the four parametric configurations after the spectrum analysis. We also model the optical mode localized sensor assuming an imperfect CROW with fabrication-imperfection-induced randomly disordered coupled resonators. The mode aliasing, common-mode rejection, signal-to-noise ratio and dual-channel calibration are discussed when the sensor is configured as a dispersive sensor.

The spectrum of the coupled ring resonators is analyzed in Section 2 to Section 2.3. The output characteristics of the coupled ring resonator under condition C. are discussed in Section 3 and validated in Section 4. The sensor performance and figure of merit are defined in Section 5. The disorder analysis is carried out in Section 6. The common-mode rejection and mode aliasing effect are discussed in Section 7 and Section 8, respectively. The signal-to-noise ratio and dual-channel calibration of the sensor are discussed in Section 9.

2. Transmission of the coupled ring resonators

By coupling two optical ring resonators together, a four-port system is usually applied as the optical add-drop filter is constructed. The structure of a four-port system with two coupled ring resonators is shown in Fig. 1.

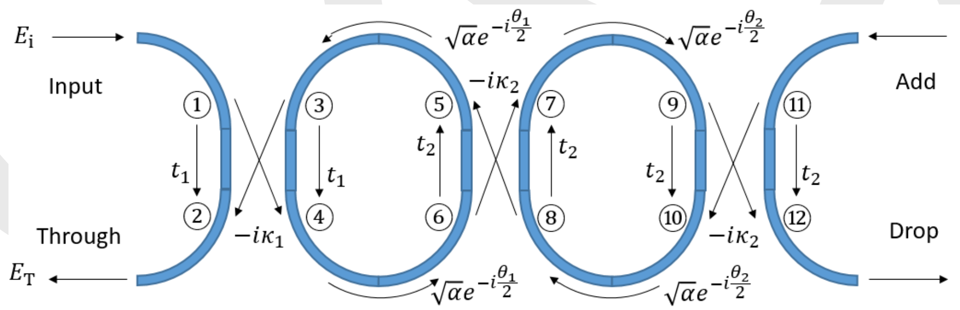

Fig. 1. A four port system constructed with two bus waveguide and two coupled ring resonators. t is the straight-through coefficient and κ the cross-coupling coefficient [13] [14]. α is the loss coefficient of the ring and zero loss is expressed by $\alpha = 1$.

In Fig. 1, every coupler is labelled with different numbered nodes to identify the details of the coupling between the bus waveguides and ring resonators. The two rings are constructed from waveguides with different propagation constants and coupled differently with bus waveguide. The relation of the electric intensity between different nodes shown in Fig. 1 can be expressed by signal flow graph as shown in Fig. 2. In Fig. 2, different phase shifts (θ_1, θ_2) of the waveguide between numbered nodes may result from different propagation constants of the waveguide or different light travel path lengths of the ring. In this paper, only the phase shift caused by different propagation constants of the waveguide is considered.

According to the feedback theory, the transfer function between the input and output of the system can be derived from:

$$G = \frac{\sum_j G_j \Delta_j}{\Delta} \tag{1}$$

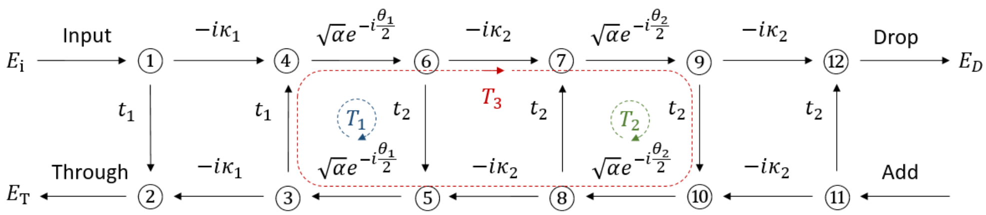

Fig. 2. Equivalent flow graph of Fig. 1. T_1, T_2 and T_3 are the three loops contained in the flow graph.

$$\Delta = 1 - \sum_m P_{m1} + \sum_m P_{m2} - \sum_m P_{m3} + \ldots \tag{2}$$

where G_j, P_{mr} and Δ_j are the gain of the jth forward path, gain product of the mth possible combination of r nontouching loops, and the value of Δ for that part of the graph not touching the jth forward path, respectively. Δ is called the determinant of the graph, and Δ_j is called the cofactor of forwarding path j [10]. The determinant of a complete flow graph is equal to the product of the determinants of each of the nontouching parts in its loop subgraph [10]. In Fig. 2, there are three individual loops denoted by T_1, T_2 and T_3 expressed by:

$$T_1 = t_1 t_2 \alpha e^{-i\theta_1};\ T_2 = {t_2}^2 \alpha e^{-i\theta_2};\ T_3 = -\kappa_2^2 t_1 t_2 \alpha^2 e^{-i(\theta_1+\theta_2)} \tag{3}$$

According to [9] and [10], the determinant of the Fig. 2 is expressed by:

$$\Delta = 1 - T_1 - T_2 - T_3 + T_1 T_2 \tag{4}$$

Here we only concern with the transmission from input to through or drop ports (only one input). The transfer function of the electric intensity from the input to the drop port and through port of the system ($G_D = E_D/E_i$; $G_T = E_T/E_i$) are expressed by:

$$\begin{aligned} G_D &= \frac{G_{1\to12}}{\Delta} \\ &= \frac{-i\kappa_1\kappa_2^2\alpha e^{-i(\theta_1+\theta_2)/2}}{1 - ae^{-i\theta_1} - be^{-i\theta_2} + (ab-c)e^{-i(\theta_1+\theta_2)}} \end{aligned} \tag{5}$$

and

$$\begin{aligned} G_T &= \frac{G_{1\to2}\Delta + G_{1\to9\to10\to2} + G_{1\to6\to5\to2}(1 - be^{-i\theta})}{\Delta} \\ &= t_1 + \frac{(d - t_1 a)e^{-i\theta_1} - t_1 be^{-i\theta_2} + (t_1 ab + f - t_1 c - db)e^{-i(\theta_1+\theta_2)}}{1 - ae^{-i\theta_1} - be^{-i\theta_2} + (ab-c)e^{-i(\theta_1+\theta_2)}} \end{aligned} \tag{6}$$

where G_D and G_T are electric intensity transfer function from the input to the drop port and through port, respectively. Parameter a, b, c, d, f are expressed by:

$$a = t_1 t_2 \alpha;\ b = t_2^2 \alpha;\ c = -\kappa_2^2 t_1 t_2 \alpha^2;\ d = -k_1^2 t_2 \alpha;\ f = k_1^2 k_2^2 t_2 \alpha \tag{7}$$

The power transmission from the input to the drop port and through port are expressed by:

$$|G_D|^2 = \frac{\kappa_1^2 \kappa_2^4 \alpha^2}{D_1 + D_2\cos(\theta_1) + D_3\cos(\theta_2) + D_4\cos(\theta_1)\cos(\theta_2) + D_5\cos(\theta_1+\theta_2)} \tag{8}$$

and

$$|G_T|^2 = \frac{N_1 + N_2 \cos(\theta_1 - \theta_2) + N_3 \cos(\theta_2) + N_4 \cos(\theta_1) + N_5 \cos(\theta_1 + \theta_2)}{D_1 + D_2 \cos(\theta_1) + D_3 \cos(\theta_2) + D_4 \cos(\theta_1)\cos(\theta_2) + D_5 \cos(\theta_1 + \theta_2)} \quad (9)$$

where $|G_D|^2$ and $|G_T|^2$ are power transmission from the input to the drop port and through port, respectively. Parameter N_x and D_x are expressed by:

$$\begin{aligned} &N_1 = (d - t_1 a)^2 + (-t_1 b)^2 + (f - db - t_1 c + t_1 ab)^2 + t_1^2; \\ &N_2 = -2(d - t_1 a)t_1 b;\ N_3 = 2[(d - t_1 a)(f - db - t_1 c + t_1 ab) - (t_1 b)t_1]; \\ &N_4 = 2((d - t_1 a)t_1 - t_1 b(f - db - t_1 c + t_1 ab));\ N_5 = 2(f - db - t_1 c + t_1 ab)t_1; \end{aligned} \quad (10)$$

and

$$\begin{aligned} &D_1 = a^2 b^2 + a^2 + b^2 + c^2 - 2abc + 1;\ D_2 = -2ab^2 + 2bc - 2a; \\ &D_3 = -2a^2 b + 2ac - 2b;\ D_4 = 4ab;\ D_5 = -2c; \end{aligned} \quad (11)$$

The power transmission of the left and right resonant peaks from $|G_T|^2$ are represented by P_T^- and P_T^+ within $-\pi < \theta < \pi$ in the transmission-phase spectrum, respectively. The power transmission of the resonant peaks from $|G_D|^2$ is represented by $P_D^\pm$. An illustration of the spectrum is shown in Fig. 3. To find the phase ($\theta_d^\pm$ and $\theta_t^\pm$) of the resonant peaks on the spectrum,

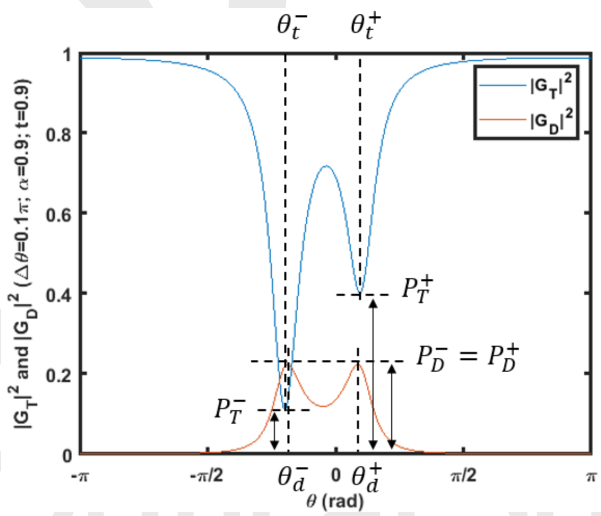

Fig. 3. Notations for resonant peaks in $|G_T|^2$ and $|G_D|^2$ with $\Delta\theta = 0.1\pi$. The power transmission of the resonant peaks are denoted by $P^\pm$ to describe resonant peaks on the left (−) and right (+) hand side. $\theta^\pm$ denotes the phase of the resonant peaks.

the extreme value of the $|G_T|^2$ and $|G_D|^2$ needs to be solved from $d(|G_x|^2)/d(\theta) = 0$. For $|G_D|^2$, the extreme values are determined from $d(|\Delta|^2)/d(\theta) = 0$, while for $|G_T|^2$, the extreme values are determined from both the denominator ($|\Delta|^2$) and numerator of Eq. (9) denoted by $|\Delta_T|^2$. $d(|\Delta|^2)/d(\theta) = 0$ and $d(|\Delta_T|^2)/d(\theta) = 0$ are expressed as:

$$D_2 \sin(\theta_1) + (D_4 + 2D_5)\sin(\theta_1 + \theta_2) = -D_3 \sin(\theta_2) \quad (12)$$

and

$$N_4 \sin(\theta_1) + 2N_5 \sin(\theta_1 + \theta_2) = -N_3 \sin(\theta_2) \quad (13)$$

The solutions from Eq. (12) are denoted by θ_d and θ_b, respectively. They correspond the local minimum and maximum of $|\Delta|^2$ solved from Eq. (12). The phase correspond to local maximum of $|\Delta|^2$ solved from Eq. (13) are denoted by θ_n.

These two equations can be treated differently corresponding to how the system is arranged. The system can be arranged into four different conditions including: A. system with zero perturbation ($t_1 = t_2, \theta_1 = \theta_2$), B. system with coupling perturbation only ($t_1 \neq t_2, \theta_1 = \theta_2$), C. system with phase perturbation only ($t_1 = t_2, \theta_1 \neq \theta_2$), and D. system with both coupling perturbation and phase perturbation ($t_1 \neq t_2, \theta_1 \neq \theta_2$). Condition A. describes the ideal initial state for sensing before any external perturbation is involved in the coupled rings. Condition C. is to apply the system as a dispersive sensor that detects the phase change of the ring resonator. In practice, condition B. can be hardly achieved since the coupling is the result of the energy exchange between the symmetrical and asymmetrical optical mode in directional couplers. Any perturbation in t is induced by perturbation in n_{eff}, which is exactly described as condition D. There is no analytical solution for a system in condition D.

If the system is lossless ($\alpha = 1$ and $t^2 + \kappa^2 = 1$), for any configurations, $|G_D|^2$ and $|G_T|^2$ have the same resonant phase ($\theta_d = \theta_b$), and they can be regarded as mirror image of each other, expressed by:

$$|G_T|^2 = 1 - |G_D|^2 \tag{14}$$

and

$$\theta_n = \theta_d = \theta_t \tag{15}$$

However, a lossless system is not practical. Here we concern about conditions A. and C. to apply the optical mode-localized sensor in dispersive sensing.

2.1. A. System with zero perturbation

Based on the system constructed with $t_1 = t_2 = t$ and $\theta_1 = \theta_2 = \theta$, the spectrum of $|G_D|^2$ can be analyzed from the denominator $|\Delta|^2$. The phase corresponding to the local maximums of $|\Delta|^2$ is solved as:

$$\begin{aligned}\theta_d &= 2m\pi \pm \left|\arccos\left[-\frac{D_2}{(D_4 + 2D_5)}\right]\right|, m \in Z \\ &= 2m\pi \pm \left|\arccos\left[\frac{t^2\alpha^2(1-\gamma)+1}{2\alpha(1-\gamma)}\right]\right|, m \in Z\end{aligned} \tag{16}$$

where θ_d denotes the phase corresponding to the resonant peaks of $|\Delta|^2$ and $\gamma = 1 - t^2 - \kappa^2$ denotes the loss of the coupler. This result indicates that two resonant peaks have the same value of $cos(\theta_d)$ and $|G_D|^2$ in a symmetrical system. The magnitude of the resonant peaks is expressed by:

$$P_D^{\pm} = |G_D(\theta_d)|^2 = \frac{\kappa^6\alpha^2(D_4 + 2D_5)}{(D_1 - D_5)(D_4 + 2D_5) - D_2^2} \tag{17}$$

The spectrum of $|G_T|^2$ needs to be analyzed from denominator $|\Delta|^2$ and numerator $|\Delta_T|^2$. The phase corresponding to the local minimum of $|\Delta_T|^2$ is solved as:

$$\theta_n = 2m\pi \pm \left|\arccos\left[-\frac{N_3 + N_4}{4N_5}\right]\right|, m \in Z \tag{18}$$

where θ_n denotes the phase corresponding to the extreme value of $|\Delta_T|^2$. Eq. (18) is different from Eq. (16) so the phase (θ_t) corresponding to the extreme value of $|G_T|^2$ exists between θ_d and θ_n ($\theta_t \in (\theta_d, \theta_n)$). This result indicates that two resonant peaks has the same value of $|G_T|^2$ in a symmetrical system and there is no analytical solution for θ_t.

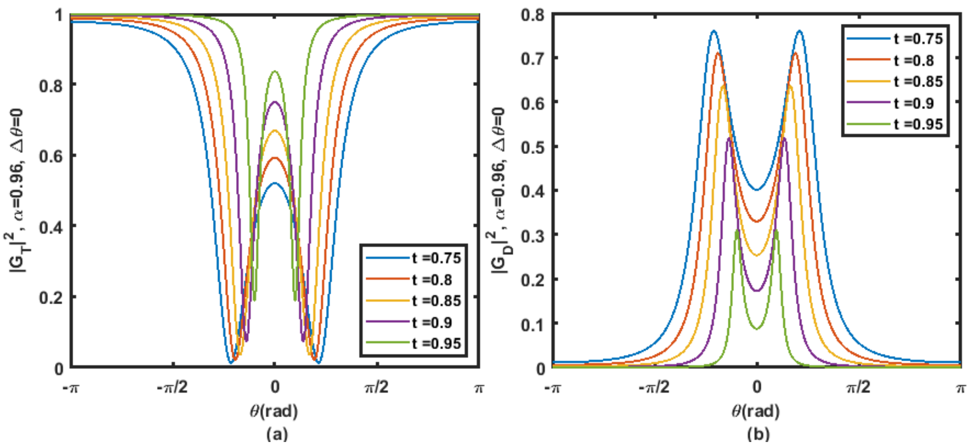

Fig. 4. Normalized power-phase spectra with $\alpha = 0.96$ and $\Delta\theta = 0$. (a). Normalized power-phase spectra from $|G_T|^2$ at different values of t; (b). Normalized power-phase spectra from $|G_D|^2$ at different values of t.

The spectrum shape of $|G_D|^2$ and $|G_T|^2$ changes with different t and α. A series of spectra from the system in condition A. with different coupling coefficients are exhibited in Fig. 4 to directly illustrate the spectrum shape. For both $|G_D|^2$ and $|G_T|^2$, higher t contributes to larger linewidth, larger separation and higher circulating power of the resonant peaks. It can be observed that θ_t and θ_d has no difference between each other. In each of $|G_D|^2$ and $|G_T|^2$, two splitting modes has identical modal amplitude. Spectra shown in Fig. 4 has the same features as derived in Eq. 16, Eq. 17 and Eq. 18.

2.2. C. System with phase perturbation

Based on system constructed from $t_1 = t_2 = t$, $\theta_1 = \theta + \Delta\theta$ and $\theta_2 = \theta$, the spectrum of $|G_D|^2$ can be analyzed from the denominator $|\Delta|^2$. The corresponding phase of the resonant peaks is solved as:

$$\begin{aligned}\theta_d &= 2m\pi - \frac{\Delta\theta}{2} \pm \left|\arccos\left[-\frac{D_2}{D_4 + 2D_5}\cos\left(\frac{\Delta\theta}{2}\right)\right]\right|, m \in Z \\ &= 2m\pi - \frac{\Delta\theta}{2} \pm \left|\arccos\left[\left(\frac{t^2\alpha^2(1-\gamma)+1}{2\alpha(1-\gamma)}\right)\cos\left(\frac{\Delta\theta}{2}\right)\right]\right|, m \in Z\end{aligned} \tag{19}$$

The two resonant peaks of $|G_D|^2$ has the same magnitude when non-identical rings coupled with bus waveguide identically. The magnitude of the resonant peaks is expressed as:

$$P_D^{\pm} = |G_D(\theta_d)|^2 = \frac{4\kappa^6\alpha^2(D_4 + 2D_5)}{[D_1 - D_5 + D_4(\cos^2(\Delta\theta/2) - 1)](D_4 + 2D_5) - D_2^2\cos^2(\Delta\theta/2)} \tag{20}$$

The spectrum of $|G_T|^2$ needs to be analyzed from denominator $|\Delta|^2$ and numerator $|\Delta_T|^2$. For $d(|\Delta_T|^2)/d(\theta) = 0$, it is hard to find analytical solutions for Eq. (13) when $\theta_1 \neq \theta_2$. If propagation and coupling loss is small ($\alpha^2 \approx \alpha$, $1-\gamma \approx 1$), an approximation can be expressed as:

$$\theta_n \approx 2m\pi - \frac{\Delta\theta}{2} \pm \left|\arccos\left[\frac{(1-\gamma_1 + t_1t_2)\alpha}{2}\cos\left(\frac{\Delta\theta}{2}\right)\right]\right|, m \in Z \tag{21}$$

A series of spectra from the system in condition C. with different coupling coefficients are exhibited in Fig. 4 to directly illustrate the spectrum shape. For both $|G_D|^2$ and $|G_T|^2$, higher

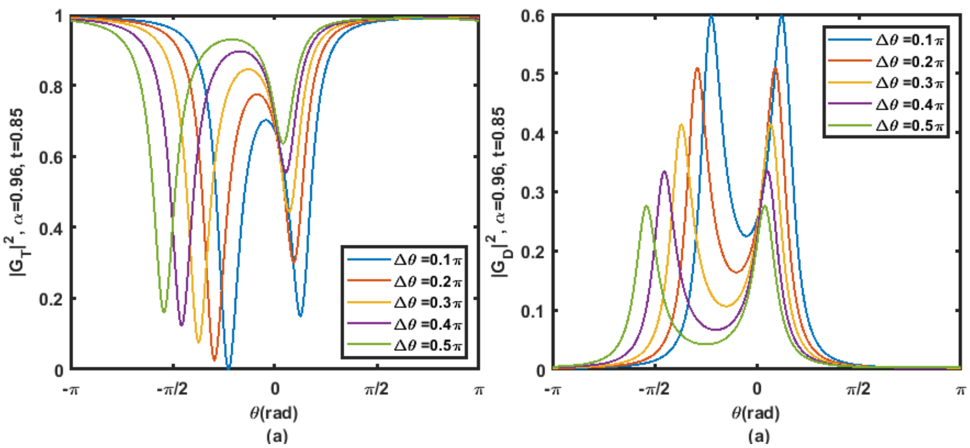

Fig. 5. Normalized power-phase spectra with $\alpha = 0.96$ and $t = 0.85$. (a). Normalized power-phase spectra from $|G_T|^2$ at different values of $\Delta\theta$; (b). Normalized power-phase spectra from $|G_D|^2$ at different values of $\Delta\theta$.

$\Delta\theta$ contributes to larger linewidth, larger separation and lower circulating power of the resonant peaks. It can be observed that θ_t and θ_d has very small differences between each other. Two resonant peaks in $|G_T|^2$ have different modal amplitude, which is the result of the phase/index perturbation as the input of dispersive sensing. On the other hand, two resonant peaks in $|G_D|^2$ have identical modal amplitude independent from phase/index perturbation. Moreover, a visible shift in spectral is induced by phase/index perturbation compared with condition A. Spectra shown in Fig. 5 has the same features as derived in Eq. 19, Eq. 20 and Eq. 21.

2.3. General feature of the power transmission under phase and coupling perturbations

A qualitative analysis of the resonant peaks in different loss, phase and coupling conditions are shown in Table. 1.

Condition	α	$\Delta\theta$	Δt	ΔP_D	ΔP_T	**Analytical** $P_D^{\pm}$	**Analytical** $P_T^{\pm}$
A	1	0	0	0	0	✓	✓
	0.96	0	0	0	0	✓	×
C	1	< 0	0	0	0	✓	✓
	1	> 0	0	0	0	✓	✓
	0.96	< 0	0	0	> 0	✓	×
	0.96	> 0	0	0	< 0	✓	×

Table 1. Summary of spectrum of $|G_D|^2$ and $|G_T|^2$ under different configurations. $\Delta\theta = \theta_1 - \theta_2$; $\Delta t = t_1 - t_2$; $\Delta P_D = P_D^- - P_D^+$; $\Delta P_T = P_T^- - P_T^+$. Column labelled with 'Analytical $P_D^{\pm}$' or 'Analytical $P_T^{\pm}$' indicates whether analytical solution existed for resonant peaks from $|G_D|^2$ or $|G_T|^2$, respectively. Here $\alpha = 1$ and 0.96 choose to illustrate the system with and without loss, respectively.

From Table. 1, $|G_D|^2$ can be precisely solved in configurations A. and C., while precise solution of $|G_T|^2$ only exists when system is lossless ($|G_T|^2 + |G_D|^2 = 1$). The precise expressions of the resonant power transmission and corresponding phases of $|G_D|^2$ only exist when the magnitude of the two resonant peaks from $|G_D|^2$ are the same. $|G_T|^2$ can be solved numerically only unless the system is lossless. In configurations A., the two resonant peaks from $|G_D|^2$ or $|G_T|^2$ have the same power transmission. However, in configuration C. the transmission of the two resonant peaks from $|G_T|^2$ is different.

For a system with loss in configurations D., the transmission of the resonant peaks from $|G_D|^2$ or $|G_T|^2$ are always different depends on the specific relation between the phase (θ_1, θ_2) and coupling coefficient (t_1, t_2).

Systems in configurations C. can be applied as sensors if the perturbation of measurand can be coupled to the perturbation in phase. The different resonant magnitude of two peaks makes it possible to be applied as an optical mode-localizer that evaluates the phase symmetry by analyzing the modal phases and powers in the spectrum. Ideally, the system with phase perturbation is better than other configurations since the asymmetric mode splitting in $|G_T|^2$ and the symmetric mode splitting in $|G_D|^2$ provide good sensitivity and noise immunity at the same time. The analytical solutions for resonant peaks in $|G_D|^2$ make the system easy to be analyzed from the measurement. In practice, rings could not have identical parameters due to fabrication imperfection.

3. Output characteristics of the dispersive sensing

Here the circuitry constructed under configuration C. is chosen to be the core sensing element. In configuration C. the magnitude of the resonant peaks of the sensing element is altered by the change of the phase change in one of the resonators. Both symmetric mode splitting from $|G_D|^2$ and asymmetric mode splitting from $|G_T|^2$ in the spectrum are helpful to simplify the post-analysis and achieve high sensitivity at the same time. The precise solutions of resonance in $|G_D|^2$ allow the propagation loss α to be measured from the magnitude of resonant peaks. The magnitude of the left and right resonant peaks from $|G_T|^2$ are represented by P_T^- and P_T^+ within $-\pi < \theta < \pi$ in the power-phase spectrum, respectively. The magnitude of the resonant peaks from $|G_D|^2$ is represented by $P_D^{\pm}$. The output of the sensing element is evaluated by the power ratio P_T^-/P_T^+. The characteristics of the circuitry with $t = 0.75$ in the range of $|\Delta\theta| < \pi$ are shown in Fig. 6 and Fig. 7.

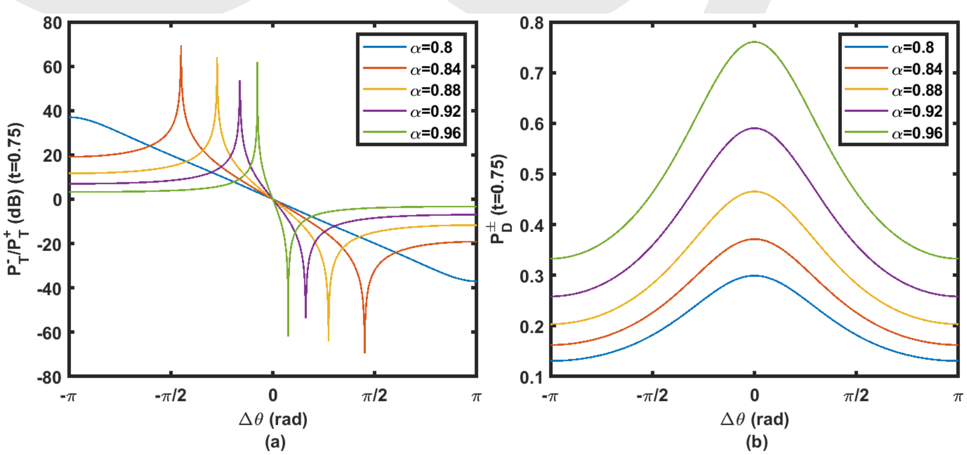

Fig. 6. (a). Power ratio (dB) between resonant peaks from $|G_T|^2$ at different values of α; (b). Normalised magnitude of resonant peaks from $|G_D|^2$.

In Fig. 6 (a), the power ratio curve is symmetrical about the origin point. Impressive values of power ratio between 50 to 70 dB are obtained from the local maximum of the curve. The accuracy of the calculated extreme values on the power ratio curves is hardly affected by numerical errors. In practice, the recognition of the local maximum and minimum of the curve are closely related to noise floor from the environment (see Section 8). It can be observed that the propagation loss coefficient α closely relates to the curve shape of power ratio P_T^-/P_T^+. The local maximum and minimum approaches to each other when the α becomes larger. The system sensitivity (slope of output) is magnified in the region between the local maximum and minimum, and it is further increased by larger α. With different values of t and α, the curve of power ratio can be negatively correlated to the phase change applied on the ring or experiencing a local maximum and minimum when phase change is negative and positive, respectively. This feature brings a problem in identifying the phase perturbation on the ring from the measured power ratio since a single value of power ratio might be corresponding to two values of the phase perturbation.

For $P_D^\pm$ shown in Fig. 6 (b), curves are symmetrical to $\Delta\theta = 0$. $P_D^\pm$ can be used to solve the value of α from the analytical solution described in Eq. (19) and Eq. (20). Moreover, $P_D^\pm$ is monotonic in the region of $-\pi < \Delta\theta < 0$ or $0 < \Delta\theta < \pi$, so the combination of P_T^-/P_T^+ and $P_D^\pm$ is necessary to obtain the right value of phase perturbation. The normalized powers of $P_T^\pm$ with $t = 0.75$ under α from 0.8 to 0.96 are shown in Fig. 7.

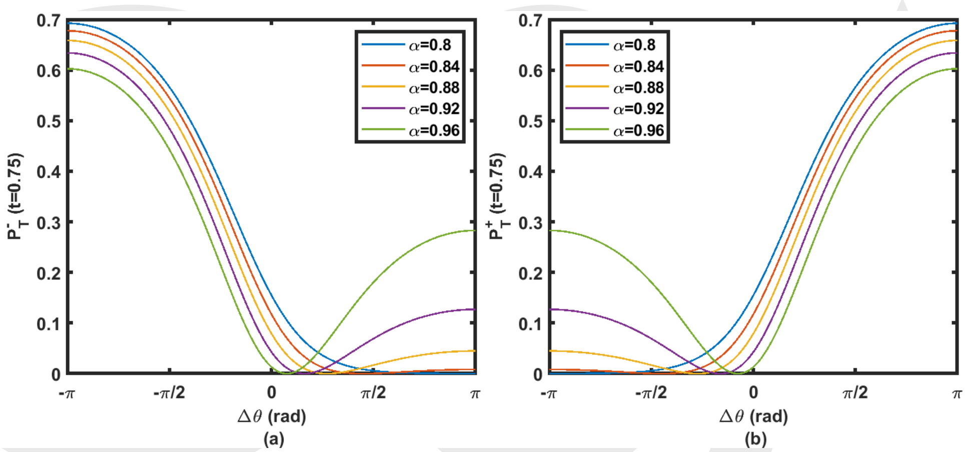

Fig. 7. (a). Normalized magnitude of P_T^- under α from 0.8 to 0.96; (b). Normalised magnitude of P_T^+ under α from 0.8 to 0.96.

From Fig. 7 (a) and (b), one local minimum can be found on each curve of P_T^- and P_T^+. For a specific combination of t and α, P_T^- and P_T^+ are symmetrical to $\Delta\theta = 0$. Local maximums and minimums in Fig. 6 (a) are the result from local minimums on the P_T^- and P_T^+ curves. When $|\Delta\theta| > \pi$, one of the resonant peaks is shifted out from the observed phase range. In this case, the P_T^- or P_T^+ from other period enters the observed phase range and relabelled as P_T^+ or P_T^-, while the previous P_T^+ or P_T^- will be relabelled as P_T^- or P_T^+ following the definition of P_T^- and P_T^+. The exchange of P_T^- and P_T^+ cause a sudden drop/raise can be observed at $\Delta\theta = \pm\pi$ in Fig. 6 (a) and Fig. 7.

$P_T^\pm$ in Fig. 7 can be also evaluated in the unit of decibel as shown in Fig. 8. One significant advantage of evaluating sensing output by power ratio P_T^-/P_T^+ rather than $P_T^\pm$ can be illustrated by comparing Fig. 8 with Fig. 6 (a). The output linearity and average sensitivity from power ratio P_T^-/P_T^+ are wonderfully improved than evaluating modal power from just one resonant peak, though the measurement range may be affected by an additional local maximum of the output.

The power ratio P_T^-/P_T^+ and normalised power $P_D^\pm$ at different t are shown in Fig. 9 and Fig. 10. By observing the power ratio P_T^-/P_T^+ under different coupling coefficients from $t = 0.75$ to $t = 0.95$, local maximum and minimum on the curve disappear when the coupling

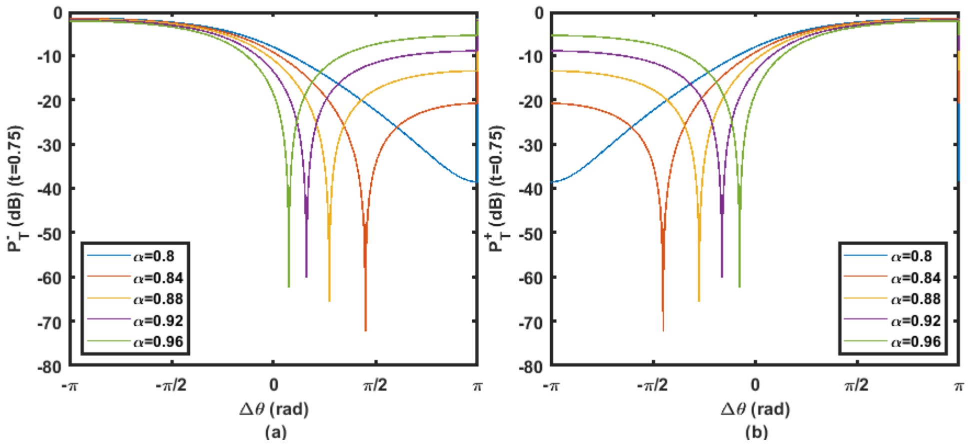

Fig. 8. (a). Normalized magnitude (dB) of P_T^- under α from 0.8 to 0.96; (b). Normalised magnitude (dB) of P_T^+ under α from 0.8 to 0.96.

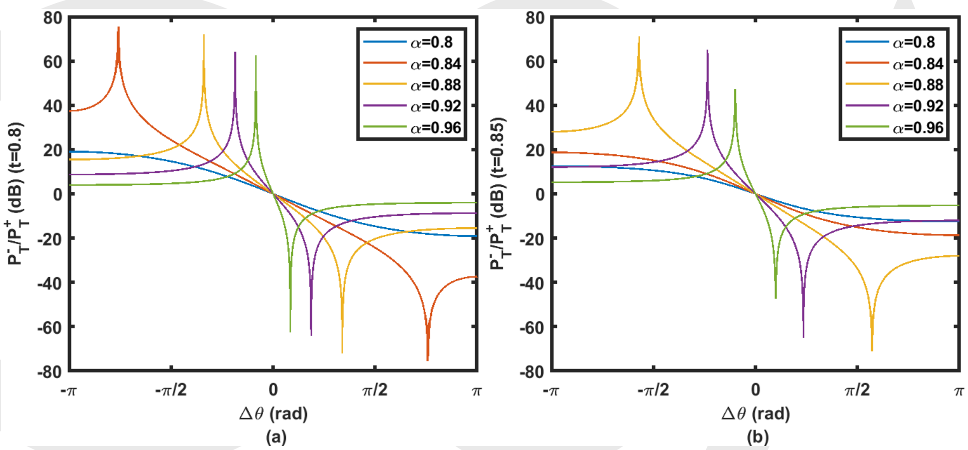

Fig. 9. Power ratio from P_T^- and P_T^+ at α from 0.8 to 0.96. (a). Power ratio (dB) ($t = 0.8$); (b). Power ratio (dB) ($t = 0.85$).

coefficient approaches or higher than loss coefficient. The system sensitivity and linearity can be adjusted according to the specific requirement on the range of $\Delta\theta$. A necessary trade-off between sensitivity and measurement range should be involved during the system design.

4. Model validation of dispersive sensing by simulation

The transmission spectrum analysis of the coupled ring resonators can also be carried out by the Lumerical interconnection module, which is capable of analyzing complicated photonic circuitry, including ring resonators. The theoretical calculation according to the signal flow graph method can be examined and validated by the simulation result. To compare the theoretical model with the simulation result, a conversion between the phase change and effective index change is necessary. If the dispersion is not involved in the consideration, the conversion can be expressed as:

$$\Delta\theta = \frac{2\pi L_0}{\lambda}\Delta n \tag{22}$$

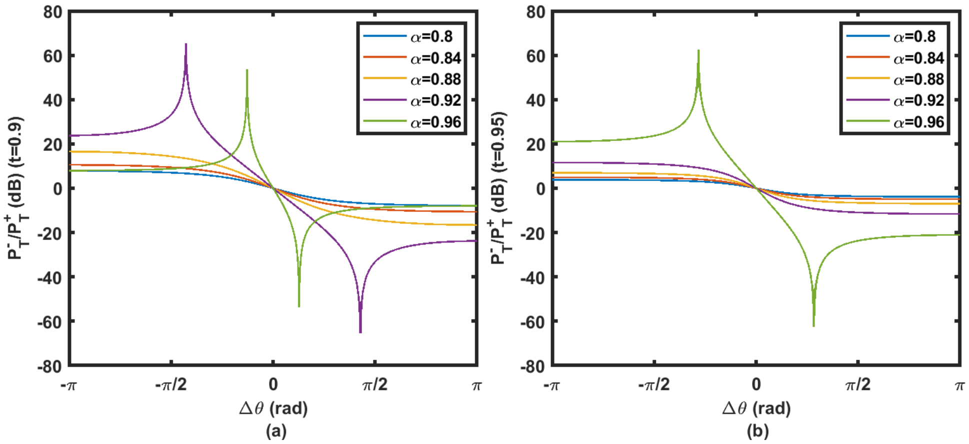

Fig. 10. Power ratio from P_T^- and P_T^+ at α from 0.8 to 0.96. (a). Power ratio (dB) (t = 0.9); (b). Power ratio (dB) (t = 0.95).

From Eq. (22), the phase perturbation ($\Delta\theta$) is not a constant in the spectrum with a constant index change (Δn), so the curve of the power ratio (P_T^-/P_T^+) versus phase perturbation must be different from the curve of power ratio versus index change (Δn). The parameters of the model used for theory validation are shown in Table. 2.

Case	n_{eff}	$L_0(\mu m)$	α	t	Loss $(1/m)$
C	1.8	280	0.96	0.9	280

Table 2. Model parameters chosen for theory validation

The propagation loss is calculated based on α and L_0. Please be noticed that t in the table is the coupling coefficient for the electric intensity and the power coupling coefficient is t^2. The calculation result from Mason's rule and Lumerical simulation are shown in Fig. 11. The

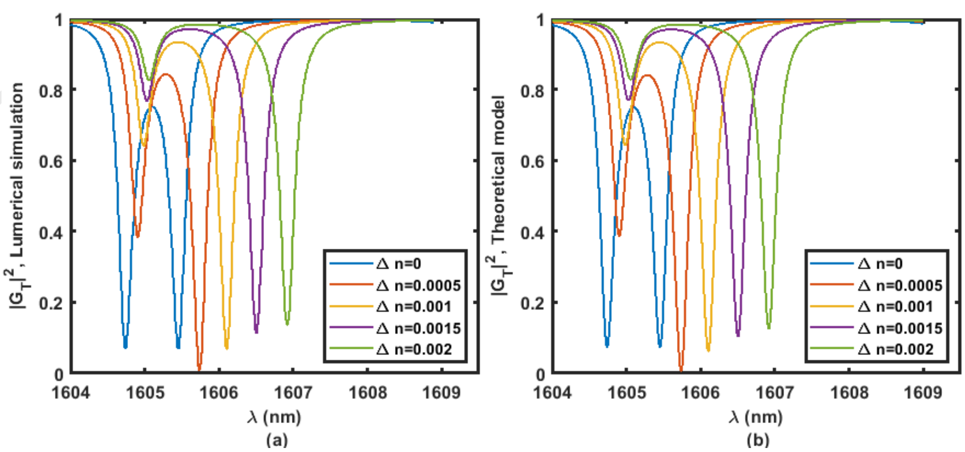

Fig. 11. $|G_T|^2$ from α = 0.96 and t = 0.9 calculated by theory model (Matlab) and Lumerical interconnection module from Δn= 0 to 0.002. (a). Lumerical simulation; (b). Theory.

calculated spectrum from signal flow graph and Lumerical simulation shows almost no visible difference in resonant frequency and amplitude in Fig. 11. The minor difference between signal flow graph and Lumerical simulation can be evaluated by comparing the power ratio (P_T^-/P_T^+) from resonant peaks shown in Fig. 12.

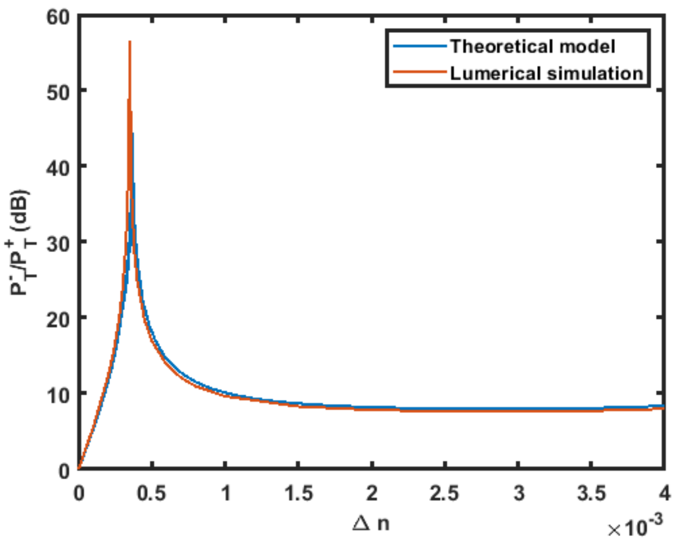

Fig. 12. Power ratio (dB) from P_T^- and P_T^+ at Δn from 0 to 0.004 (0 to π).

There is a slight difference between curves in Fig. 12 except the region near the peak of the power ratio. Generally, the analysis from both methods is consistent with each other. The simulation result appears to be less affected by the numerical errors during the calculation rather than the calculation result from Matlab. The Lumerical interconnect module simulates the light travelling in the given photonic circuitry until the energy in the circuitry attenuates to a preset value (approaching zero). The process allows the calculation to be carried out with less numerical approximation than the derived transfer function that contains few exponential terms (Taylor expansion required). This unique feature of the Lumerical interconnection can be understood as an advantage when high accuracy analysis is required in complex photonic circuitry.

5. Figure of merits

The sensing performance can be briefly described by linear sensitivity S (dB/rad), saturated power ratio R^s (dB), peak phase θ^p (rad), peak output R^p (dB) and linear region LR (rad) as shown in Fig. 13. According to the output characteristics of the system (Section 3), θ_t^p and R_t^p shown in Fig. 13 may not exist when t is larger than α as in Fig. 9 and Fig. 10 so the most important parameters are the linear sensitivities S and saturated power ratios R^s in $|G_T|^2$ and $|G_D|^2$. A rough shape of the sensing output curve can be simply constructed from S_t and R_t^s. The sensing output range of the device is decided by saturated range $2R_t^s$ or peak-to-peak range $2R_t^p$ depending on whether the local maximum/minimum exists. The linear sensing region LS is located between two intersecting points of saturated power ratios R^s and linear sensitivity S, which is labelled out in Fig. 13. Here the performance of the optical mode localized dispersive sensors by saturated range, peak-to-peak range, linear region LR and linear sensitivity S. We therefore define an FOM for CROW mode localized sensing as the product of linear region and

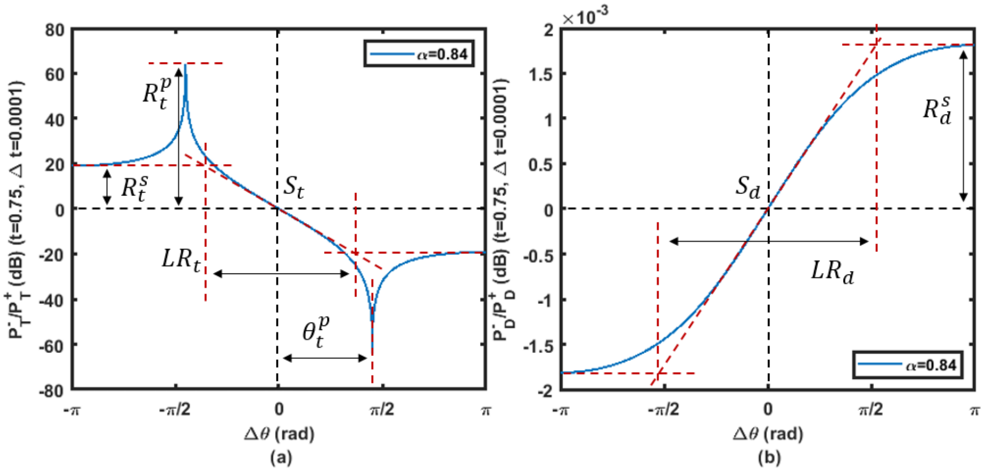

Fig. 13. Notations for figure of merits of the sensing output. (a). The power ratio curve of $|G_T|^2$ can be briefly described by S_t, R_t^s, θ_t^p and R_t^p. (b). The power ratio curve of $|G_D|^2$ can be briefly described by S_d and R_d^s. The value of S_d and R_d^s will be zero if the system is in condition C. The curve shown here is the result of perturbation in both index and coupling coefficient (condition D.). The linear sensing region LR is located between two intersecting points of saturated power ratios R^s and linear sensitivity S.

sensitivity:

$$FOM = LR \times S \tag{23}$$

FOM defined in Eq. (23) represents the balance between the sensitivity and linear region of the sensor. A high value of FOM indicates the sensor is well designed when a specific requirement on LR or S is reached.

6. Disorder analysis

The possible disorders in t and α induced by fabrication imperfection are analyzed with the reference of [15]. The analysis is carried out by applying random perturbations (Δt and Δn) on the reference device designed with $t = 0.8$, $\alpha = 0.97$ and $n_{eff} = 1.839$. The system performance is analyzed by using 200×200 combinations of Δt and Δn to test the output characteristics. Here R_t^p is not interested since it will not appear in all the power ratio curves and it is strongly affected by numerical error. The distribution of the perturbations is shown in Fig. 14.

Details of the performance errors corresponding to Δt and Δn are shown in Fig. 15. In Fig. 15 (a) and (b), Δn has a larger weight in producing errors in θ_t^p than Δt from colour pattern, while Δt and Δn have the same chance to produce an error in S_t. In Fig. 15 (c) and (d), Δt has a larger weight in producing errors in S_d and R_d^s than Δn. In Fig. 15 (e), Δt has a larger weight in producing errors in R_t^s than Δn. In summary, S_d, R_d^s and R_t^s are sensitive to Δt. θ_t^p is sensitive to Δn. S_d is sensitive to both Δt and Δn. The errors in performance caused by random disorders are shown in Table 3.

In Table 3, the calculated performance errors are always less than 6% in 90 % coverage of all random data. This number indicates that the fabrication of the optical mode localized sensor is possible.

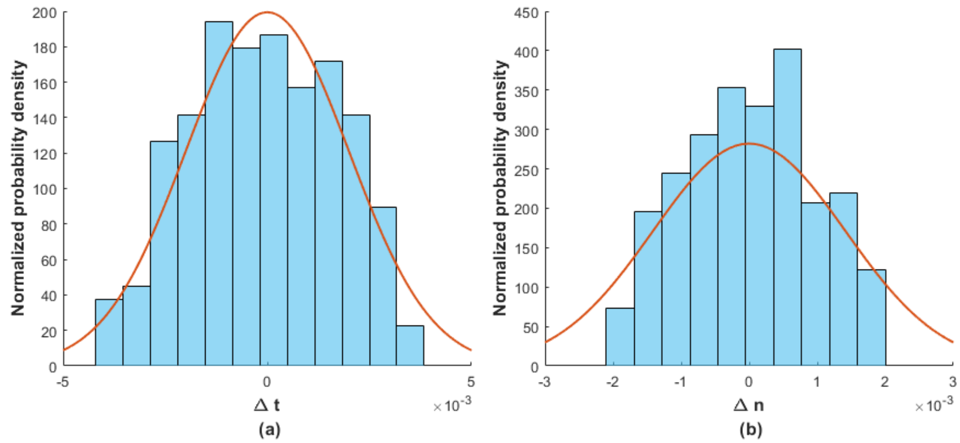

Fig. 14. Randomly generated coupling and index perturbations. (a). Gaussian fit of Δt, mean=± 0.004 and standard deviations=0.004×10^{-3}. (b). Gaussian fit of Δn, mean=± 0.002 and standard deviations=0.002×10^{-3}.

Sensing performance errors		
Parameters	**90% data around $\Delta t = \Delta n = 0$**	**100% data around $\Delta t = \Delta n = 0$**
Δn	± 0.0012	± 0.002
Δt	± 0.00196	± 0.004
$\Delta \theta_t^p$	$\pm 3\%$	$\pm 6\%$
ΔS_t^p	$\pm 6\%$	$\pm 15\%$
ΔR_t^s	$\pm 1.5\%$	$\pm 3.5\%$
ΔS_d(dB/rad)	± 0.045	± 0.11
ΔR_d^s(dB)	± 0.08	± 0.12

Table 3. Errors of random disorder on sensing performance. The reference value of R_d^s and S_d is 0 dB and 0 dB/rad, respectively, so ΔR_d^s and ΔS_d is not shown in percentage.

7. Common-mode rejection

In practice, thermal-optic effect [16] and waveguide dispersion [17] will affect resonant wavelength and magnitude of resonant peaks in silicon photonics devices, respectively. For ring resonators, the spectrum shift caused by the thermal-optic effect is not negligible as a result of the enhanced circulating power in the ring. Dispersion in the waveguide will influence the resonant wavelength in the spectrum as well. Meanwhile, the magnitude of resonant peaks will not be affected by the thermal-optic effect and dispersion, which means the output characteristics defined by the resonant modal power ratio will not be affected by the thermal-optic effect and dispersion. Any external perturbation that is applied to two resonant peaks in common-mode will be rejected by evaluating the power ratio as sensing output. This is the common-mode rejection feature of the optical mode-localized sensing.

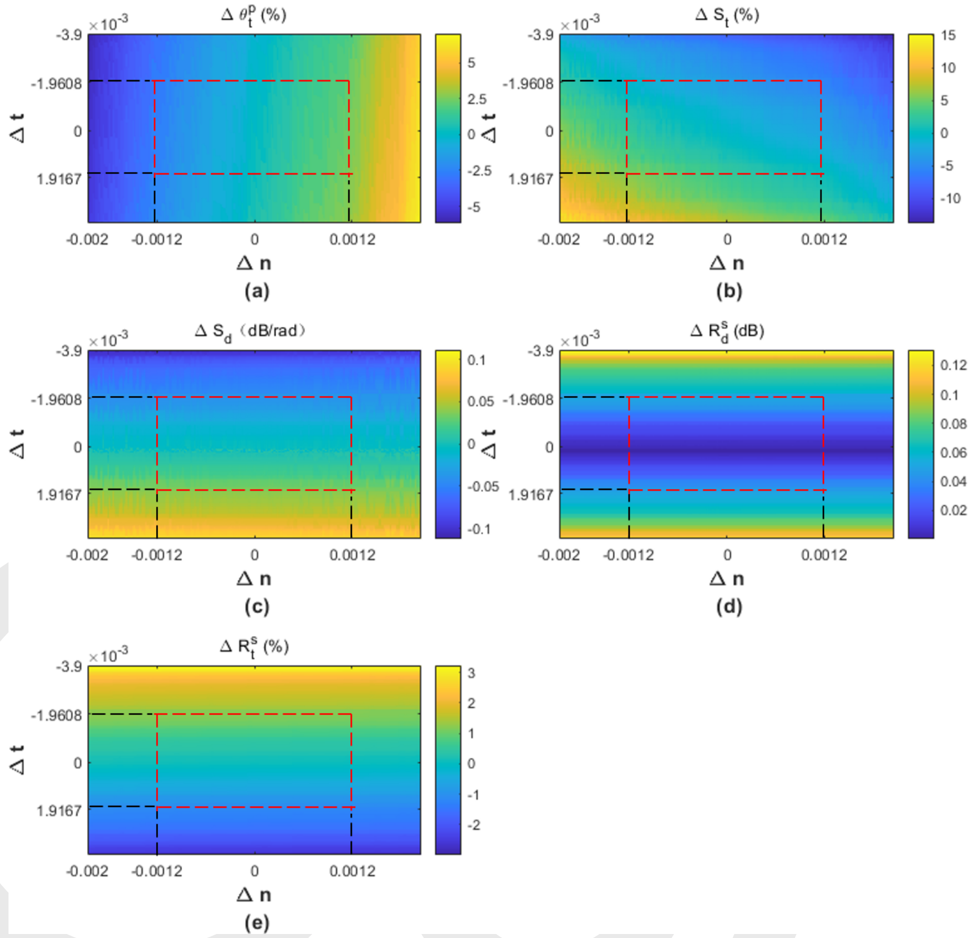

Fig. 15. The performance errors induced by Δt and Δn. The red box covers the area where 90% of the data points are located. (a). $\Delta\theta_t^p$(%). (b). ΔS_t(%). (c). ΔS_d(dB/rad). (d). ΔR_d^s(dB). (e). ΔR_t^s(%).

8. Mode aliasing

The overlap of the modes disrupts the recognition of the modal amplitudes of the two resonant modes if the modes' frequencies are close to each other. The failure of the mode recognition produces a 'sensing dead zone' around the point of zero perturbation. The sensitivity gets worse when the resonant line-width is enlarged by damping. The overlap of these two modes is referred to as the mode aliasing effect [18]. Unlike mechanical mode localized sensor, the mode aliasing only happens when the sensor is constructed with some specific combination of t and α. Recalling the modal phase of $|G_D|^2$ in Eq. (19), a small phase difference between two resonant modes is obtained from high t and low α. Therefore, mode aliasing can be avoided by selecting a suitable value of t and α within the whole spectrum. For instance, the system with $t = 0.97$ has the mode aliasing when $\alpha \leq 0.8$ in $|G_D|^2$ and $\alpha \leq 0.68$ in $|G_T|^2$ as shown in Fig. 16.

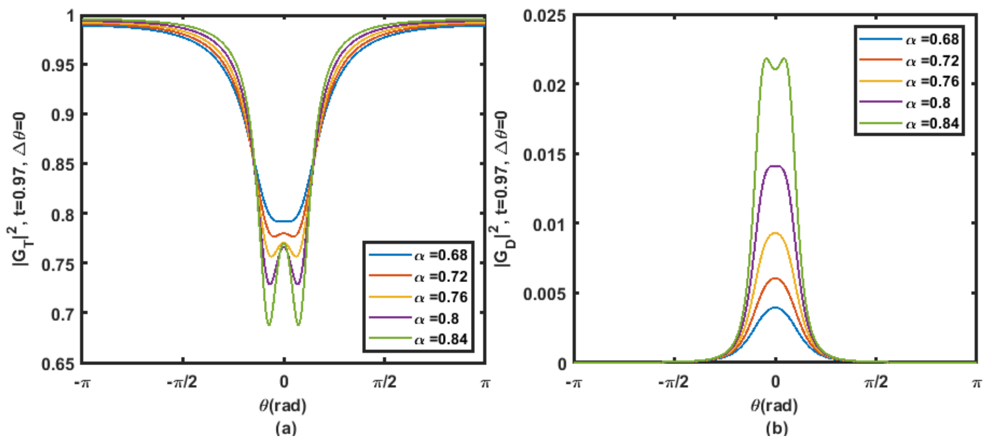

Fig. 16. Illustration of mode aliasing. (a). $|G_T|^2$ with $t = 0.97$ and α from 0.68 to 0.84. (b). $|G_D|^2$ with $t = 0.97$ and α from 0.68 to 0.84.

9. Signal-to-noise ratio and dual-channel calibration in configuration C.

The detectable value of the maximum and minimum power ratio in the system is determined by SNR from $|G_T|^2$ and $|G_D|^2$. Following the definition of SNR [18]:

$$\mathrm{SNR_T} = \frac{P_T^-}{P_T^+} / \frac{P_n^-}{P_n^+} \tag{24}$$

$$\mathrm{SNR_D} = 1 / \frac{P_n^-}{P_n^+} \tag{25}$$

where P_n^- and P_n^+ represent the noise on the resonant peaks. From Eq. (24), $\mathrm{SNR_T}$ is getting worse when $P_T^- < P_T^+$, while Eq. (25) indicates that $\mathrm{SNR_D}$ only depends on the noise power ratio. The combination of the resonant peaks in $|G_T|^2$ and $|G_D|^2$ can improve the SNR of the sensor when $P_T^- < P_T^+$. This SNR compensation technique is the unique feature of the optical mode localization rather than a mechanical one. The measured power of the two resonant peaks from $|G_T|^2$ and $|G_D|^2$ are expressed as:

$$P_{Tm}^{\pm} = P_T^{\pm} + P_n^{\pm} \tag{26}$$

$$P_{Dm}^{\pm} = P_D^{\pm} + P_n^{\pm} \tag{27}$$

where $P_{Tm}^{\pm}$ and $P_{Dm}^{\pm}$ represent the measured power of resonant peaks in $|G_T|^2$ and $|G_D|^2$, respectively. By resolving the measured resonant peaks in $|G_T|^2$ and $|G_D|^2$ separately, two different phase perturbation values can be solved out. These two values define a range where the noiseless phase perturbation locates, thus the sensing accuracy is improved, and a real-time measurement error is quantified as well.

Here we name this unique technique dual-channel calibration. This dual-channel calibration of the optical mode localization sensing mechanism makes it better than the mechanical mode localization sensing mechanism in a noisy environment.

10. Conclusion

The mode localization in coupled optical ring resonators is analyzed with Mason's signal flow graph in configuration A and C, corresponding to the system with no perturbation, perturbation in effective index, respectively. A simple qualitative analysis about the resonant peaks in different loss, phase and coupling conditions is concluded. The analytical model of the coupled ring resonators is examined by Lumerical simulation. The calculation result from the simulation is slightly different from the analytical model due to the numerical errors.

The coupled ring resonators in configuration C is considered a good choice for sensing application due to the unique output spectrum among other configurations. The optical mode localization sensing can achieve high sensitivity due to the high modal power ratio between two resonant peaks. The linearity and sensitivity is improved by regarding the modal power ratio compared with the modal power from one of the peaks, and the unexpected common-mode perturbation can be rejected as well. The linear sensing range and linear sensitivity of the sensor can be adjusted by different combinations of t and α. A trade-off between the linear sensing range and linear sensitivity must be considered in practical applications. The figure of merit is defined as the product of the linear sensing range and sensitivity to describe the excellence of the performance.

Based on the four-port structure originate from the add-drop filter, two output spectrums with mode localization and symmetric mode splitting provide a new dimension for signal analysis. Combining the two spectrums allows the high-sensitivity sensing and dual-channel calibration to be carried out simultaneously, which can reduce the sensing errors. Monte-Carlo analysis is carried out to find out how the sensing performance is affected by perturbation from fabrication imperfection. The results show that the fabrication imperfection changes less than 6% of the performance in 90% cases.

It is proved that the optical mode localized sensing has advantages in sensitivity, accuracy and anti-aliasing compared with conventional mode localization one. Various types of high-sensitive sensors can be constructed through coupling parametric perturbation (Δt and $\Delta\theta$) with measurands in different physical domains. Unlike mechanical mode localized sensing, standard packaging is applicable for optical mode localized sensing in most applications rather than vacuum packaging, which makes the optical mode localized sensor a better candidate for commercialization.

Funding. Engineering and Physical Sciences Research Council (funding body EPSRC EP/V000624/1).

Acknowledgments. The authors thank silicon photonics group for necessary guidance and assistance in the simulations. This work was supported by the Engineering and Physical Sciences Research Council under funding body EPSRC EP/V000624/1.

Disclosures. The authors declare no conflicts of interest.

Data Availability Statement. Data underlying the results presented in this paper are not publicly available at this time but may be obtained from the authors upon reasonable request.

References

1. M. Spletzer, A. Raman, A. Q. Wu, X. Xu, and R. Reifenberger, "Ultrasensitive mass sensing using mode localization in coupled microcantilevers," Appl. Phys. Lett. **88**, 254102 (2006).
2. P. Thiruvenkatanathan, J. Yan, and A. A. Seshia, "Common mode rejection in electrically coupled mems resonators utilizing mode localization for sensor applications," in *2009 IEEE International Frequency Control Symposium Joint with the 22nd European Frequency and Time forum,* (IEEE, 2009), pp. 358–363.
3. C. Zhao, M. H. Montaseri, G. S. Wood, S. H. Pu, A. A. Seshia, and M. Kraft, "A review on coupled mems resonators for sensing applications utilizing mode localization," Sensors Actuators A: Phys. **249**, 93–111 (2016).
4. J. K. Poon, J. Scheuer, S. Mookherjea, G. T. Paloczi, Y. Huang, and A. Yariv, "Matrix analysis of microring coupled-resonator optical waveguides," Opt. express **12**, 90–103 (2004).
5. V. Y. Venediktov, Y. V. Filatov, and E. V. Shalymov, "Passive ring resonator micro-optical gyroscopes," Quantum Electron. **46**, 437 (2016).
6. Z. Yao, K. Wu, B. X. Tan, J. Wang, Y. Li, Y. Zhang, and A. W. Poon, "Integrated silicon photonic microresonators: emerging technologies," IEEE J. Sel. Top. Quantum Electron. **24**, 1–24 (2018).
7. S. Feng, T. Lei, H. Chen, H. Cai, X. Luo, and A. W. Poon, "Silicon photonics: from a microresonator perspective," Laser & photonics reviews **6**, 145–177 (2012).
8. A. Yariv, "Universal relations for coupling of optical power between microresonators and dielectric waveguides," Electron. letters **36**, 321–322 (2000).
9. S. J. Mason, "Feedback theory-some properties of signal flow graphs," Proc. IRE **41**, 1144–1156 (1953).

10. S. Jung, I. Song, and J. D. Cressler, “Systematic methodology for applying mason’s signal flow graph to analysis of feedback circuits,” in *2014 IEEE International Symposium on Circuits and Systems (ISCAS),* (IEEE, 2014), pp. 2421–2424.
11. S. Mandal, K. Dasgupta, T. Basak, and S. Ghosh, “A generalized approach for modeling and analysis of ring-resonator performance as optical filter,” Opt. communications **264**, 97–104 (2006).
12. S. Dey and S. Mandal, “Modeling and analysis of quadruple optical ring resonator performance as optical filter using vernier principle,” Opt. Commun. **285**, 439–446 (2012).
13. L. Chrostowski and M. Hochberg, *Silicon photonics design: from devices to systems* (Cambridge University Press, 2015).
14. A. Yariv and P. Yeh, *Photonics: optical electronics in modern communications*, vol. 6 (Oxford university press New York, 2007).
15. J. Wang, Z. Yao, T. Lei, and A. W. Poon, “Silicon coupled-resonator optical-waveguide-based biosensors using light-scattering pattern recognition with pixelized mode-field-intensity distributions,” Sci. reports **4**, 1–9 (2014).
16. R. Amatya, C. W. Holzwarth, M. Popovic, F. Gan, H. Smith, F. Kartner, and R. Ram, “Low power thermal tuning of second-order microring resonators,” in *2007 Conference on Lasers and Electro-Optics (CLEO),* (IEEE, 2007), pp. 1–2.
17. M. L. Cooper, G. Gupta, M. A. Schneider, W. M. Green, S. Assefa, F. Xia, D. K. Gifford, and S. Mookherjea, “Waveguide dispersion effects in silicon-on-insulator coupled-resonator optical waveguides,” Opt. letters **35**, 3030–3032 (2010).
18. C. Zhao, G. S. Wood, J. Xie, H. Chang, S. H. Pu, and M. Kraft, “A force sensor based on three weakly coupled resonators with ultrahigh sensitivity,” Sensors Actuators A: Phys. **232**, 151–162 (2015).